Laser-induced modification of the patellar ligament tissue: comparative study of structural and optical changes

Author:

Ignatieva, NY; Guller, AE; Zakharkina, OL; Sandnes, B; Shekhter, AB; Kamensky, VA; Zvyagin, AV

Laser-induced modification of the patellar ligament tissue: comparative study of structural and optical changes

Natalia Yu. Ignatieva · Anna E. Guller · Olga L. Zakharkina · Bjornar Sandnes · Anatoly B. Shekhter · Vladislav A. Kamensky · Andrei V. Zvyagin

Abstract The effects of non-ablative infrared (IR) laser treatment of collagenous tissue have been commonly interpreted in terms of collagen denaturation spread over the laser-heated tissue area. In this work, the existing model is refined to account for the recently reported laser-treated tissue heterogeneity and complex collagen degradation pattern using comprehensive optical imaging and calorimetry toolkits. Patella ligament (PL) provided a simple model of type I collagen tissue containing its full structural content from triple-helix molecules to gross architecture. PL ex vivo was subjected to IR laser treatments (laser spot, 1.6 mm) of equal dose, where the tissue temperature reached the collagen denaturation temperature of $60\pm2°C$ at the laser spot epicenter in the first regime, and was limited to $67\pm2°C$ in the second regime. The collagen network was analyzed versus distance from the epicenter. Experimental characterization of the collagenous tissue at all structural levels included cross-polarization optical coherence tomography, nonlinear optical microscopy, light microscopy/ histology, and differential scanning calorimetry. Regressive rearrangement of the PL collagen network was found to spread well outside the laser spot epicenter (>2 mm) and was accompanied by multilevel hierarchical reorganization of collagen. Four zones of distinct optical and morphological properties were identified, all elliptical in shape, and elongated in the direction perpendicular to the PL long axis. Although the collagen transformation into a random-coil molecular structure was occasionally observed, it was mechanical integrity of the supramolecular structures that was primarily compromised. We found that the structural rearrangement of the collagen network related primarily to the heat-induced thermo-mechanical effects rather than molecular unfolding. The current body of evidence supports the notion that the supramolecular collagen structure suffered degradation of various degrees, which gave rise to the observed zonal character of the laser-treated lesion.

Keywords Non-ablative laser treatment · Collagen denaturation · Patellar ligament · Differential scanning calorimetry · Optical coherence tomography · Second harmonic generation microscopy · Histology

N. Y. Ignatieva
Department of Chemistry, Lomonosov Moscow State University,
Moscow, Russia

A. E. Guller · A. B. Shekhter
I.M. Sechenov First Moscow State Medical University,
Moscow, Russia

N. Y. Ignatieva · O. L. Zakharkina
Institute on Laser and Information Technologies of RAS,
Troitsk, Russia

B. Sandnes · A. V. Zvyagin (✉)
MQ Photonics Centre, Macquarie University,
Sydney NSW 2109, Australia
e-mail: andrei.zvyagin@mq.edu.au

V. A. Kamensky
Institute of Applied Physics of RAS,
Nizhniy Novgorod, Russia

B. Sandnes
Department of Physics, University of Oslo,
PO Box 1048, Blindern,
N-0316, Oslo, Norway

Introduction

A rapidly growing field of medical laser applications calls for better understanding of laser-tissue interactions despite its extensive research development over the last few decades [1]. Therapeutic laser treatment of the connective tissue pathologies [2–4], fractional photothermolysis, and resurfacing [5, 6] in the non-ablative regime represent important examples of laser application in medicine. At the

same time, the primary effect of the non-ablative laser treatment is often confined to that of the laser-induced heat. It has been accepted that this heat causes thermal denaturation (unfolding) of collagen [2–4, 7, 8], which is one of the most important constituents of the connective tissue, responsible for its structural integrity and biomechanical properties. The existing model of the laser-induced collagen denaturation assumes uniform heating, where molecular mechanisms [9–12], thermodynamic parameters [12, 13], and kinetic properties [13, 14] of collagen denaturation are well known. Tissue architecture, however, has been observed to influence the thermal field distribution in tissue, as demonstrated in the study of the laser- and heat-induced effects in annulus fibrosus [15], which motivates a refinement of the existing model by taking into account the complex spatial temperature distribution in the collagenous tissue under treatment.

We address this problem by carrying out a systematic study of the collagenous tissue remodeling caused by the IR non-ablative laser treatment under clinically relevant conditions. A preliminary account of this work has been reported elsewhere [15]. *Patella ligament* provided an excellent tissue model due to its exquisitely ordered, anisotropic structure of collagen [16, 17], which would highlight any structural disorders. In order to highlight the laser-induced collagen thermal denaturation effects, two temperature regimes were chosen: $T < T_d$ and $T \cong T_d$, where T represents the peak temperature of the laser-treated tissue, and T_d is the denaturation temperature of the PL collagen under uniform heating. The structural modifications of the collagenous tissue at different levels of its hierarchical organization were explored using the following experimental methods. Bright-field light microscopy (LM) in combination with histological and histochemical staining provided a clinically accepted "gold standard" for the assessment of the structural and functional state of the tissue at the macro- and micron-scale levels. Second harmonic generation (SHG) microscopy provided superior sensitivity of the fibrillar helical structures. The SHG process is particularly efficient in type I collagen due to its high non-linear susceptibility [18]. Cross-polarization optical coherence tomography (CP-OCT) measured the local reflectivity of the tissue at the resolution of tens of microns. In addition, CP-OCT probed the alignment order and integrity of the collagenous tissue by analyzing the polarization state of the reflected light [19–21]. We also employed differential scanning calorimetry (DSC) to determine the triple-helical molecule content of the sample. The sample and a reference were heated simultaneously, while monitoring power supplied to both to maintain equal temperature. An endothermic event in the sample, such as the denaturation occurring at T_d, absorbs an amount of heat equal to the enthalpy (ΔH) value associated with the

collagen rearrangement. ΔH and T_d variations reflect alterations in collagen organization on the molecular and supramolecular level [10–12].

Materials and methods

Animal sample preparation procedure

Twenty 5-month-old Chinchilla male and female rabbits, weight range 2,100–3,300 g, were used in this experiment in accordance with the ethics committee protocol for animal experiments of I.M. Sechenov First Moscow State Medical University, Russia. The animals were originally used for an unrelated spine surgical study, and eventually killed by intravenous injection of 100 mg/kg body weight of phenobarbital sodium into the medial auricular vein. Fresh rabbit knee joint complexes consisting of a lower fragment of femur bone, a quadriceps tendon, patella, patellar ligament, and the upper fragment of tibia bone were harvested within 2 h after euthanasia of animals. Adjacent muscular tissue, fat and synovial lining were removed to isolate the patellar ligament. The knee joint complexes were stored in 0.15-M NaCl at room temperature until the laser-treatment procedure, but not longer than 1 h. The fully hydrated complexes without any blotting were mounted in a custom jig. The samples were exposed to dry air during the laser treatment and optical coherence tomography measurements. Special care was exercised to keep the sample hydrated during all procedures, so that even during the longest optical coherence tomography imaging procedure the sample exposure to air was less than 1 min, thus eliminating dehydration-induced measurement artifacts. The laser-treated sample thickness was 1.3±0.1 mm, with length and width 14.5±0.1 mm and 6.0±0.5 mm, respectively.

Laser treatment

An Er:glass fiber laser (IRE-POLUS Co., Fryazino, Russia) was used as the heating source. Light of wavelength λ=1.56 μm was delivered via a 600-μm quartz optical fiber normally to the posterior PL surfaces forming a circular spot of 1.6-mm diameter measured as full width at half maximum (~2% of the total tissue surface area). The effective penetration depth of the laser light was evaluated using the following parameter used in the light transport equation, in the diffusion approximation, to describe the optical response of the tissue: $\sigma_{eff} = (3\mu_a[\mu_a + \mu_s(1 - g)])^{-1/2}$, in terms of its absorption μ_a and scattering μ_s coefficients, respectively, g – anisotropy factor. $\sigma_{eff} \cong 0.8$ mm for the relevant values of μ_a= 9.65 cm^{-1}, μ_s=60 cm^{-1}, g=0.97 for collagenous tissue [15]. The fiber tip was held at a distance of 5 mm from the

sample surface by means of a custom-made mount. The laser-treatment ratings and corresponding treatment groups, designated as L_1 and L_2, are listed in Table 1. In particular, the laser exposure times were 4 s for L_1 and 2 s for L_2 (irradiances 25 W/cm^2 and 50 W/cm^2, respectively).

Temperature acquisition

Spatial temperature distribution during the laser irradiation was monitored by a thermograph IRTIS-2000 (IRTIS Ltd., Moscow, Russia) in the IR spectral band of 3-5 μm at an angular resolution <2 mrad. The laser-heated area was imaged onto the thermograph sensor via a lens, and read out in two modes: frame-scan or line scan at rates of 1 Hz or 60 Hz, respectively. In the line-scan mode, the temperature was sampled along the radial line either parallel or perpendicular to the PL axis during the laser heating and cooling, with a typical heating-cooling pattern presented in Fig. 1.

Laser-treated samples

The total number of laser-treated samples was 15 and 11 for L_1 and L_2 treatment groups, respectively, whereas five untreated samples were used as control samples (Table 1). These PL samples were dissected followed by immediate characterization using DSC, and, at a later stage, LM, and SHG imaging. CP-OCT images were acquired before and after the laser treatment at a fixed lateral position with respect to the PL sample over a time interval of 10–60 s.

Morphological investigation and specimen preparation

Morphological assessment of the PL samples was carried out using LM examination of the conventional (5 μm in thickness) and semi-thin (1 μm in thickness) histological preparations, and also using SHG imaging and analysis. The laser-treated tissue was sampled at a depth range of 150 μm–1 mm.

All morphological samples were divided into two batches. In the first batch, the samples were fixed in buffered formalin, dehydrated in graded series of alcohols, embedded in paraffin wax. Section cuts of 5 μm and 23 μm were used for conventional histological examination and

Table 1 Treatment groups and the laser irradiation parameters

Group	Laser radiation dose, J/cm^2	Exposure time, s	Number of experiments
L_1	100	4	15
L_2	100	2	11
Control			5

SHG microscopy, respectively. The 5-μm paraffin slices were stained with hematoxylin and eosin (H&E). The samples for SHG imaging remained unstained.

In the second batch, the samples were prepared as semi-thin slices. Immediately after harvesting, small tissue fragments were fixed in the Ito's solution at a temperature of 4°C for at least 48 h, subsequently washed in 0.1-M sodium cacodylate buffer (pH 7.2–7.4), and post-fixed with 1% osmium tetroxide in the same buffer for 1 h. The samples were dehydrated in graded alcohols and embedded in epoxy resin. The tissue blocks were cut using an ultra microtome (LKB, Bromma, Sweden) into serial semi-thin sections of 1-μm thickness, and stained with methylene blue (azure II) basic fuchsine threechrome method (MAFT), according to the conventional protocol.

Light microscopy

The H&E-stained and semi-thin histological preparations were examined by an upright light microscope (Olympus BX51) using dry-air (4×/NA0.10; 10×/NA0.25; 20×/NA0.40) and oil-immersion (100×/NA1.25 oil) objectives (Olympus Optical, Tokyo, Japan). Histology images were recorded using a digital video camera (640×480, Sanyo Electric Co., Ltd., Osaka, Japan) in a single-frame mode.

Second harmonic generation microscopy

SHG images were acquired using a Leica DM IRBE/TCS SP2 confocal/nonlinear laser scanning microscope (Leica Microsystems GmbH, Wetzlar/Mannheim, Germany) (Fig. 2).

An infrared, femtosecond titanium-sapphire laser (Tsunami, Spectra Physics, Newport Corporation, Irvine, CA, USA), pumped by a 5-W diode laser (Millennia, Spectra Physics, Newport Corporation, Irvine, CA, USA), provided the excitation beam (power at the sample, 10 mW), at a wavelength of λ_{ex}=870 nm, which was focused in the sample using a PL APO 40×/1.25 oil-immersion Objective (Olympus Optical, Tokyo, Japan) and raster-scanned across it to form an *en face* image. Laser pulsewidth at the microscope input port ranged from 80 to 150 femtoseconds (fs), at a repetition rate of 80 MHz. The nonlinear laser scanning microscope captures *en face* optical sections of approximately 2 μm in thickness. Forward-propagating SHG photons at a wavelength of $\lambda_{ex}/2$=435 nm were collected using a high-NA oil-immersion condenser, spectrally filtered using a filter cube, and detected using a photomultiplier tube (PMT) detector in transmission configuration (Fig. 2c). The filter cube was fitted with: (1) a short-pass filter (SP 700 nm) to block the fundamental laser excitation (cut-off, 700 nm); (2) dichroic mirror (DC 560 nm) to split the SHG and TPF components;
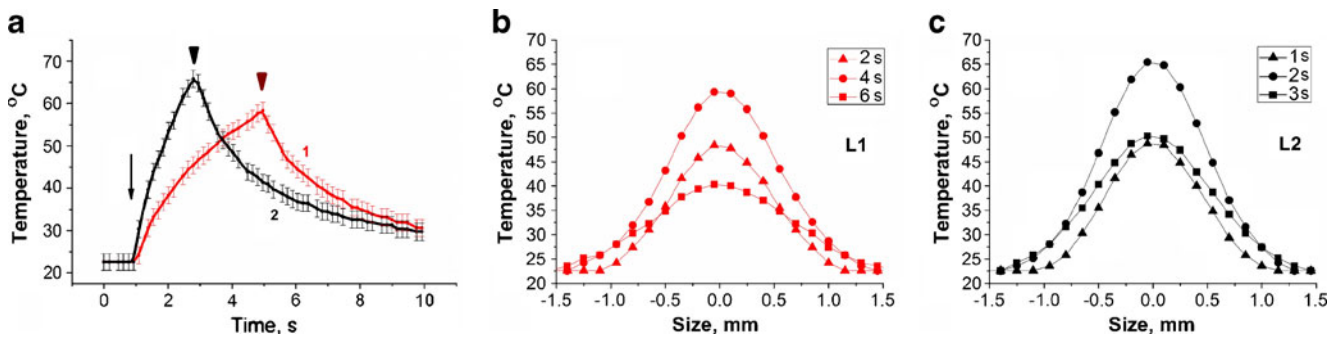
Fig. 1 **a** Temporal dependence of temperature at the epicenter of the laser spot during the PL tissue treatment. Curves 1 and 2 relate to L_1 and L_2 laser-treatment groups, respectively. The *arrow* and *arrowheads* demarcate laser turn on and turn off times, respectively. The thermograph was run at 60-Hz line-scan rate. **b**, **c** Temperature maps of the PL tissue during and after the L_1 L_2 laser treatment, respectively

and (3, 4) band-pass filters of the wavelength transmission range of 395–440 nm to pass SHG (BP 395–440 nm), and TPF (BP 573-648 nm) signals, respectively. The SHG image pixel size was 1024×1024 pixels corresponding to a scan area of size 375 μm×375 μm.

Morphometry

The LM and SHG images of the control and laser-treated PL-samples (total, 569) were quality-sorted (442 images), classified into 27 groups using tissue treatment, sample preparation, imaging method, and tissue zone classifiers. Random sampling of 30% images of each classified group yielded 131 images for morphometric analysis, which was performed using a standard statistical program packet SPSS 13.0 for Windows (SPSS Inc., Chicago, IL, USA).

Cross-polarization optical coherence tomography

We employed a CP-OCT system developed at the Institute of Applied Physics of RAS (Nizhny Novgorod, Russia) that has been described elsewhere [21]. Briefly, the system consisted of a scanning low-coherence interferometer illuminated with a broadband polarized light source wavelength centered λ_0=980 nm (bandwidth, $\Delta\lambda$= 45 nm). The CP-OCT produced a sample cross-section reflectivity map (imaging depth, ~1 mm), sampled with the (longitudinal) in-depth and transverse resolutions of 15 μm and 25 μm, respectively, as shown in Fig. 3, with logarithm-base-ten of the local sample reflectivity coded in color. Since the CP-OCT signal was polarization-sensitive, it was possible to analyze the polarization state of the reflected light by processing two orthogonally
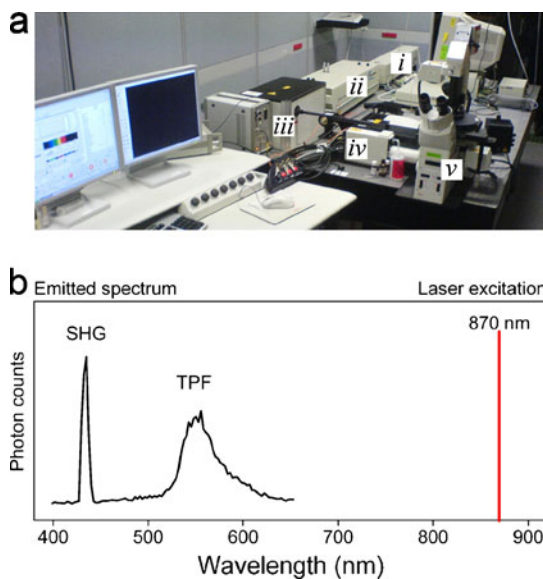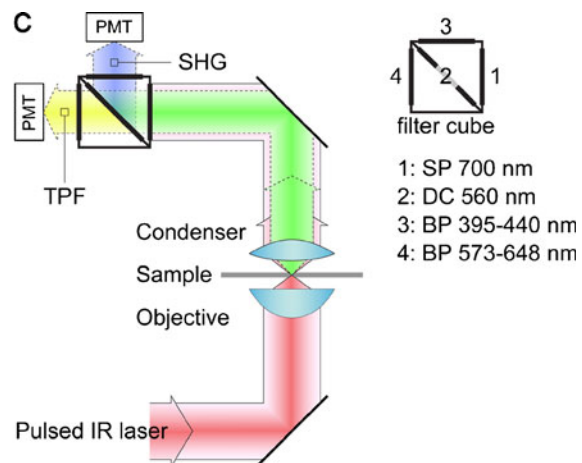

Fig. 2 Experimental setup for second harmonic generation (SHG) imaging. **a** Photograph of the laboratory room showing (i) pump laser, (ii) femtosecond pulsed IR laser (fs-laser), (iii) beam alignment, (iv) confocal scanning module, and (v) inverted microscope. **b** Emission spectrum of the collagenous tissue excited by the fs-laser. SHG signal is spectrally narrow, whereas two-photon excited fluorescence (TPF) signal is broadband and red-shifted. **c** The microscope optical configuration (see text for details)
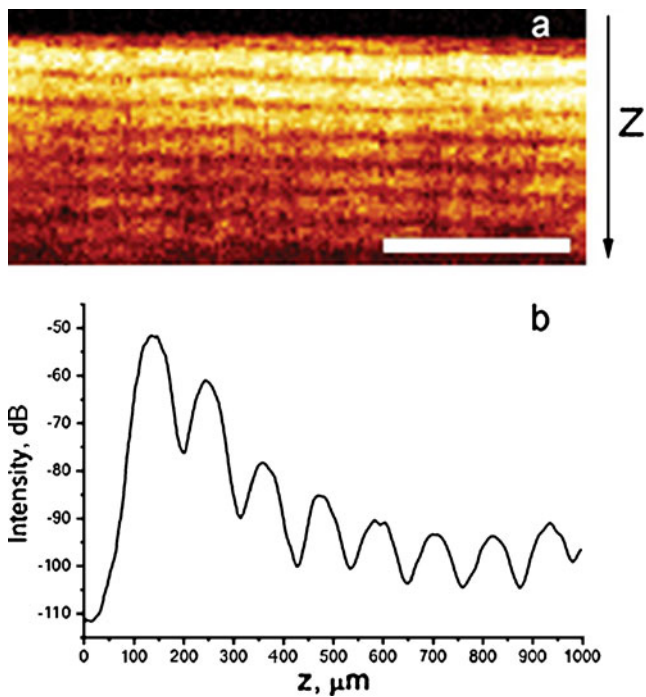
Fig. 3 **a** Typical CP-OCT image of intact PL showing a banding pattern that reports on the tissue birefringency. **b** An averaged cross-section profile of the image (**a**) along the optical z-axis (in depth). *Scale bar*, 500 μm

polarized signals received in the dual detection arm of the CP-OCT interferometer. The resultant signal is expressed as

$$S \propto A(z) \cos[4\pi \Delta n z / \lambda_0], \qquad (1)$$

where A is the local reflectivity strength of the sample, and Δn the birefringence index. As it is evident from Eq. (1), local tissue birefringence can be determined by this system. If Δn is constant throughout the sample, S oscillates along the z-axis, with period, $z_b = \lambda_0 / (2\Delta n)$ giving rise to the "banding pattern" seen in Fig. 3 [21] .

Differential scanning calorimetry (DSC)

The calorimetric measurements were carried out using a DSC instrument (Mettler-Toledo GmbH, Schwerzenbach, Switzerland). A tissue specimen of mass, m_s=4-6 mg, and volume $2 \times 2 \times 1$ mm^3, was placed in the 40-μl hermetically sealed aluminum pan, with an empty pan used as a reference, and heated at the rate of 10°C/min from temperature T=25 to 95°C. The data were acquired by averaging over at least three runs for each representative sample type, followed by immediate hydrolization of the specimens and assaying for collagen content. The raw data were analyzed with the Star^e software (Mettler-Toledo Inc., Columbus, OH, USA) to obtain the onset and peak temperatures (T_{onset}, and T_{peak}, respectively) and $\Delta W = W_s - W_r$ where W_s and W_r is the heat power

flowing into the sample and reference, respectively, in order to maintain their equal predetermined temperature during the DSC scan. A DSC plot of the untreated collagenous tissue sample, ΔW versus T is shown in Fig. 4a. The denaturation enthalpy ΔH_d per unit mass (J/kg) was defined as $K \times A$, where K is the calorimetric constant, and A is the area under the curve, and normalized for the collagen mass of the sample. The skewness index was calculated as $SI = \Delta H_i / \Delta H_d$, where ΔH_i was determined for the temperature range $T_{onset} < T < T_{peak}$ [12]. Comparing the denaturation enthalpy before and after the sample thermal treatment, ΔH_d and ΔH, respectively, collagen denaturation percentage was calculated as $\alpha = (1 - \Delta H / \Delta H_d) \cdot 100\%$.
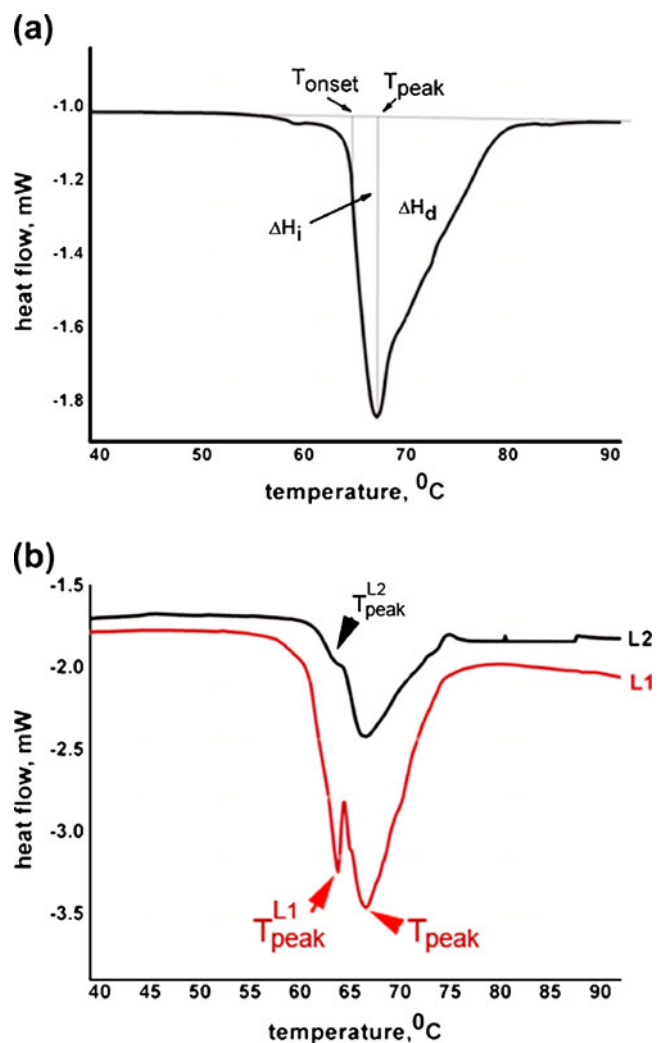

Fig. 4 Typical differential scanning calorimetry thermograms of the patellar ligament **a** intact, and **b** after the laser-treatment. DSC parameters, T_{onset}, T_{peak}, ΔH_d and ΔH_i are defined in the text. The DSC curves measured for the laser-treated PL are noticeably different from the intact PL (compare with **a**). Note a low temperature peak (L_1) and pronounced shoulder (L_2 group)

Biochemical analysis

The analysis of the amino acids of the hydrolyzed tissue was performed using an amino acid analyzer (Hitachi Ltd., Ibaragi, Japan). The molar ratios of hydroxylysine/hydroxyproline and glycine/alanine used as the collagen type classifier were 14.5 and 2.77, respectively. These values indicated that the rabbit PL main content was type I collagen [22],[23]. Hydroxyproline is a collagen-specific amino acid that made up 13.5% of the collagen molecule. The total collagen content of the rabbit PL was found to account for $86\pm2\%$ and about 98% of the tissue and protein dry weight, respectively.

Results

Intact patellar ligament tissue

The intact PL tissue was characterized by the hierarchical organization of collagen fibers, fascicles, and bundles (Fig. 5a, b), with collagen bundles connected laterally forming sheets. The fascicles were separated by fibroblasts (tenocytes), featuring dark-stained thread-like nuclei. The endotendineum sheaths containing spindle and rounded-shape fibroblasts, blood vessels, and rare lymphocytes and macrophages, rendered bundle borderlines distinguishable. Quasi-periodic domains of both smooth longitudinal waves and angular crimps were observed. The SHG images revealed high-contrast, bright features of collagen origin, as shown in Fig. 5c. The fascicles were barely discernable as a wavy ribbon motif due to merging into bundles via lateral connections. The endotendineum sheaths produced a weak or undetectable SHG signal (negative contrast) resulting in clear delineation of the PL collagen bundles. Waviness and angular crimps of the collagen were clearly revealed in the SHG images. Low-frequency spatial intensity modulation of the SHG signal across the image was due to the orientation of the collagen fibrous structures relative to the axis of the incident light polarization [18].

As discussed above, the CP-OCT in-depth reflectivity signals were modulated (Fig. 3) due to the birefringence (an optical analog of anisotropy) of the highly ordered, surface-parallel collagen structure running along the preferential axis, called the long axis. This periodic modulation was laterally uniform across the intact PL specimen producing a banding pattern (Fig. 3a). An in-depth periodicity of the CP-OCT, $n\cdot z_b$ was measured to be 103 ± 2 μm (Fig. 3b) yielding $z_b=71\pm2$ μm assuming the tissue refractive index, $n=1.45$ [24]. Using Eq. (1), the birefringence index of the intact PL was calculated to be $\Delta n=(6.9\pm0.2)\times10^{-3}$.

In the DSC experiment, a strong sharp peak (endotherm) observed in the thermograms of the intact PL (Fig. 4a) was related to the denaturing process, a transition of the collagen macromolecules from their native triple helical structure into a more random "coiled" structure via unfolding. ΔH_d, T_{onset} and T_{peak} were measured to be 63 ± 3 J/g, 64.0 ± 0.5 and $67.0\pm0.5°C$, respectively. SI was calculated to be 0.29 ± 0.03.

Effect of laser irradiation

The temperature time evolution of the samples at the laser irradiation epicenter exposed to the equal-dose laser radiation (100 J/cm^2) of different exposure times 4 s (L$_1$) and 2 s (L$_2$) are shown in Fig. 1. Temperature peaks were detected at $60\pm2°C$ and $67\pm2°C$ for the L$_1$ and L$_2$ laser-treatment groups, respectively.

The temperature was sampled at a subsurface tissue layer of $\sigma_{IR}=1/\mu_{IR}<100$ μm, where σ_{IR} and μ_{IR} are effective photon penetration depth and effective attenuation coefficients at the thermograph operation wavelength range [15]. So, the measured radiometric quantity provided temperature readout averaged over σ_{IR}, which was under-
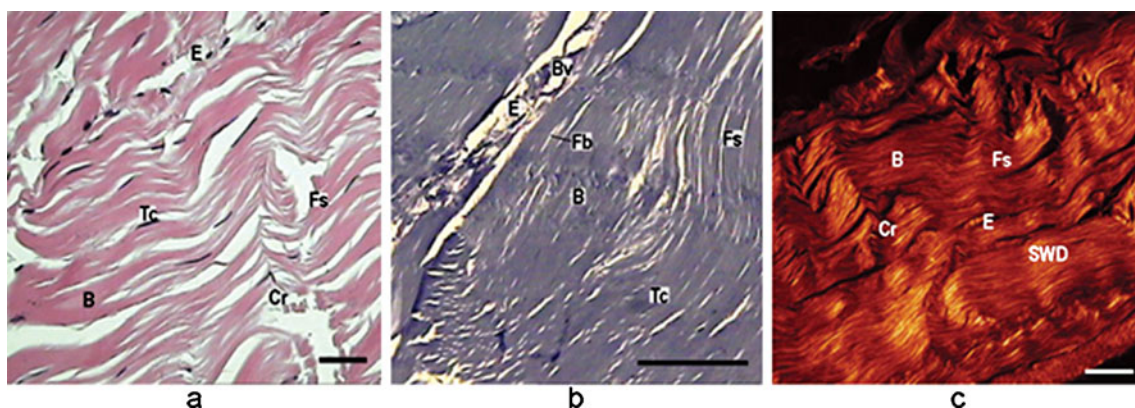

Fig. 5 Optical images of intact PL showing the hierarchical organization of the collagen structures. Light microscopy images of the a, b histology samples, a H&E staining, 400×; b semi-thin slice, MAFT staining, 1000×; and c SHG image of the unstained sample. The incident light polarization axis is directed horizontally. *Scale bar*, 50 μm

estimated, with the most reliable maximum readout at the laser spot epicenter. The laser-treated tissue isotherms measured immediately (16 ms) after the laser action in the superficial layer (<100 μm) of tissue, were circular, in qualitative agreement with the optical diffusion theory. This circular optical field distribution in the tissue was due to the considerable (tissue water) absorption, μ_a that dominated the tissue effective scattering μ_s' at the wavelength of 1.56 μm ($\mu_a \cong 5\mu_s'$, where $\mu_s' = \mu_s(1 - g)$ [15]). In order to verify this observation, we inspected the temperature field using a thin 1-mm PL tissue slice that was laser-irradiated on the front side, and temperature distribution measured on the back side, as shown in Fig. 6c, inset. The field distribution was approximately circular, as shown in Fig. 6c (slightly extended along the PL axis, ellipticity 1.2). The peak temperature on the back side did not exceed 42°C for L_1.

Based on our results and analysis, four laser-treatment zones were identified using the following classifiers: specific tissue architecture; cellular population (phenotypes, pathology degree, and damaged-to-intact cell ratio); and

ellipticity degree (with the long axis oriented perpendicular to the PL axis). Note that the zonal classification was applicable to both L_1 and L_2 sample treatment groups, as schematically presented in Fig. 6, whereas scaling and some morphological modifications were specific to the treatment group. Based on the histology analysis, these tissue zones were, from the epicenter outwards: Z_1, homogenous; Z_2, heterogeneous; Z_3, crimped; Z_4, distended tissue; followed by intact PL, as shown in Fig. 6. Temperature values acquired immediately after the laser was turned off are also indicated in the sketch at several representative sites.

Figure 7 presents high-resolution LM and SHG images of the treated PL tissue sampled in the demarcated zones shown in Fig. 6. Since individual fibers and fascicles were largely unresolved in the Z_1 histology specimens, it was termed the homogenous tissue zone (Fig. 7a, i). Here, the bundles of collagen were conjectured only due to the blood vessel remnants at the broken endotendineum sheath sites. Angular crimps and smooth wavy collagen fascicles/ bundles were not observed. Most tenocytes were necrotic
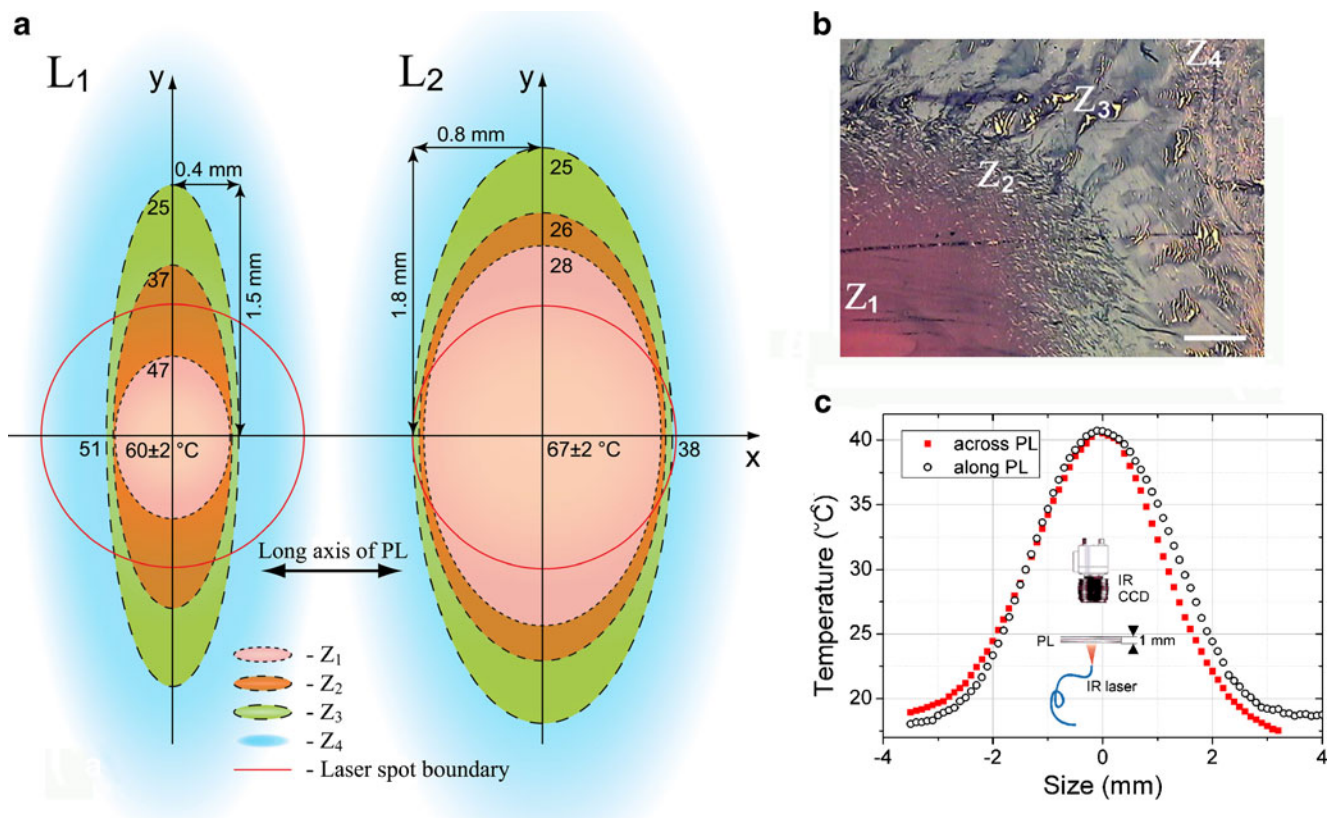

Fig. 6 a Schematic diagram and b histology image of the laser-treated PL tissue zones in the treatment groups: L_1 (*left diagram*), L_2 (*right diagram*, and picture b). Zonal demarcation (*color*): Z_1 (*pink*), homogeneous; Z_2 (*orange*), heterogeneous; Z_3 (*green*), crimped; Z_4 (*blue*), distended tissues. Local temperature values recorded immediately (16 ms) after the laser treatment are shown (all values in °C). Histology image (**b**): L_2 group sample, semi-thin slice, MAFT staining, magnification, 200×. *Scale bar*, 200 μm. **c** Plot of the temperature profiles of the laser-heated tissue spot recorded in the radial direction parallel (along PL) and perpendicular to PL (across PL) axis. *Inset*: *IR CCD* infrared CCD camera, with a lens; *PL* patella ligament tissue of thickness 1 mm; *IR laser* Er:glass infrared fiber laser
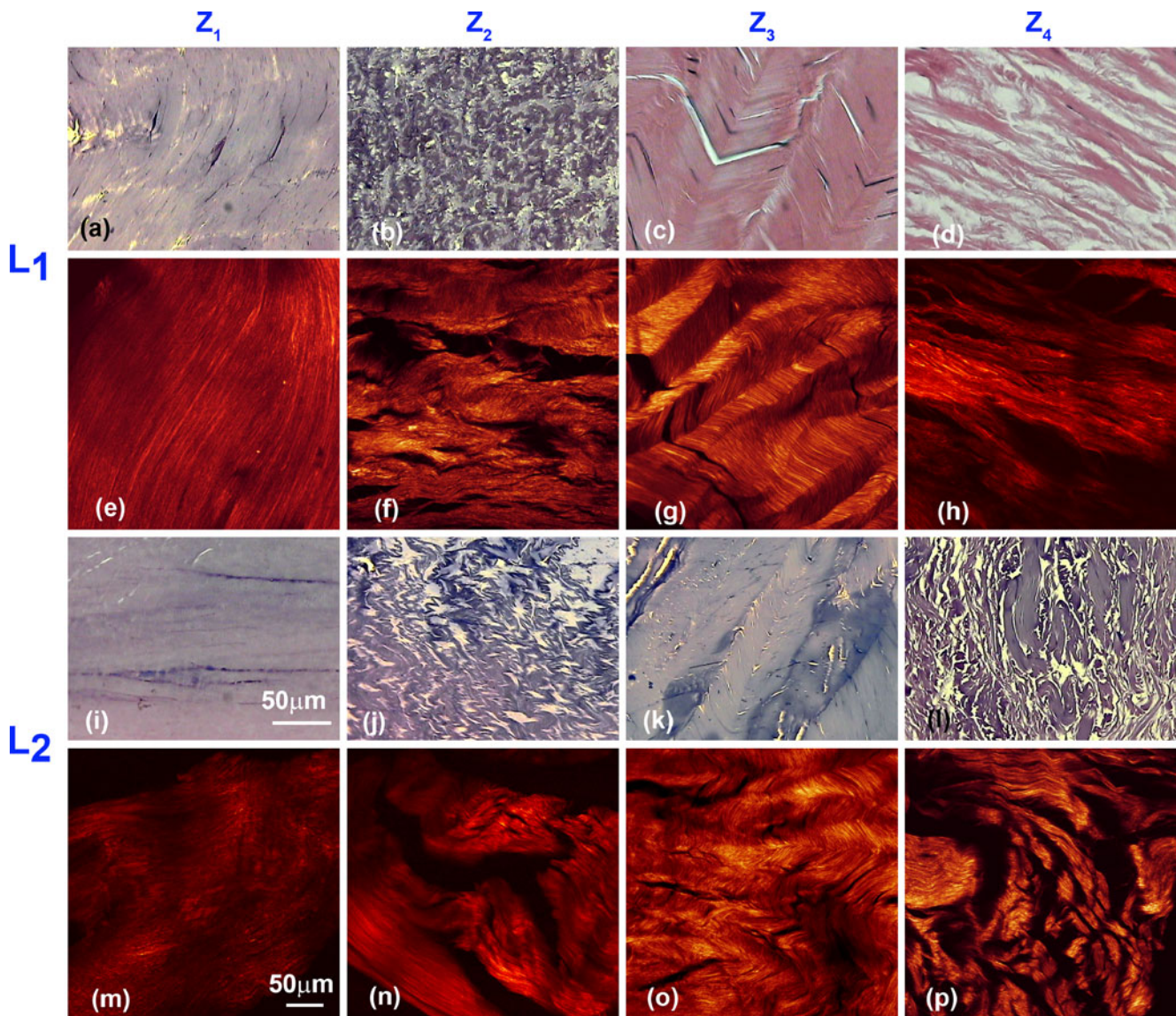
Fig. 7 LM (Histological) and SHG images of the zone fragments, corresponding to, in column-wise order, homogeneous (Z_1), heterogeneous (Z_2), crimped (Z_3), distended (Z_4) tissues. L_1, L_2 denote, in dual LM/SHG row-wise order, the corresponding treatment groups, respectively. *Scale bar*, 50 μm. All histology samples, but **c**, **d**, semi-thin preparations, MAFT staining, magnification, 1000×. **c**, **d**, H&E staining, 1000×

or paranecrotic. Homogenization was more severe in L_2 than in L_1 treatment group, where a larger proportion of cells were undamaged.

The SHG images taken in Z_1 showed a drastic reduction of contrast and overall signal degradation (Fig. 7e, m), with disordered signal distribution, including diffuse featureless areas, and sparse collagen fibers. The overall SHG contrast and collagen filament extension was greater in L_1 than in L_2.

The heterogeneous tissue zone, Z_2 spread outward from the boundaries of zone Z_1; its outer boundary shaped as an ellipse, as shown in Fig. 6 for both L_1 and L_2. In the histology specimens, dark-stained twisted/bended 3–6-μm-thick collagen fibrous structures separated by pale-colored homogenous background material sized 5-10 μm were observable, with few individual collagen fibers (Fig. 7b, j). Apical angles of the bending points of the twisted fibrous structures were different in L_1 and L_2 groups estimated as 66.7 ± 17.1 and $42.5 \pm 5.0°$, respectively. The cells were partly damaged expressing signs of karyorrhexis. Neither crimps nor endotendineum sheaths were found.

In Z_2, the SHG images were quasi-uniform and noticeably brighter exhibiting high contrast (Fig. 7f, n) compared to Z_1, and comparable to the intact PL images. This zone was populated with large-scale distinct structures, or macro-complexes. There were randomly oriented collagen filaments and fragments, and poorly defined fascicles inside the macro-complexes.

In Z_3, the angular crimp motif (collagen sheets bent at an acute apical angle) emerged. This motif was expressed more profoundly than in the intact PL. At the same time, the larger-scale smooth wavy motif disappeared. Individual collagen fibers were poorly distinguishable by LM. The tenocytes were flattened, and so were their nuclei running alongside the fascicles in the bundle mainstream (Fig. 7c, k). In Z_3, spacing between the bending points of the adjacent crimps (a crimping period) and an apical angle of the crimps in L_2 group were similar to these observed in the intact PL, as suggested by statistical (Mann–Whitney U test) analysis. In contrast, the crimping period and acuteness of the crimp apical angles were increased in L_1.

The collagenous structures produced high-contrast SHG signals resembling that of the intact PL, except for the signal intensity, which was notably greater in Z_3. Contrary to the LM data, the fibers inside the fascicles and bundles appeared well discernible in the SHG images. The crimp motif of triangular shape was clearly visualized in both L_1 and L_2 (Fig. 7g, o). The SHG tissue images in L_1 differed from that in L_2 only morphometrically.

Zone Z_4 represented the penumbra of the laser treatment, with poorly defined boundaries, as schematically shown in Fig. 6. It contained loose heterogeneous tissue gradually transforming into intact PL. Irregular tissue fragments randomly filled with distended or split fibrous structures of faint histological staining were found in Z_4, together with intact tissue fragments. L_1 and L_2 treatment group images displayed little difference (Fig. 7d, l), except for, in L_2, where, occasionally, bundles and fascicles fragments appeared homogenous. Intact PL isles gradually populated the zone towards its outer boundary. The angular crimp, smooth wavy motifs, and endotendineum structures were not observable. The tenocytes cells appeared normal, although slightly reduced in number.

The SHG signal brightness varied, often abruptly, across the images from levels comparable to that of intact PL, and attributed to the intact PL, to background noise in both L_1 and L_2 (Fig. 7h, p). These negative-contrast sites were identified as ruptures or splitting of fascicles and bundles. Intact PL isles featured diffuse edges. The angular crimps were not detected.

The laser-irradiated region was clearly defined in the CP-OCT images (Fig. 8). In L_1, the birefringence distribution across the tissue and contrast appeared to be mostly retained, except at the epicenter of the laser treatment where the banding period increased in comparison with that of the intact PL samples, with $\Delta n = (2.5 \pm 1) \times 10^{-3}$ (Fig. 8a, b). In L_2, the CP-OCT images demonstrated an overall expansion of the laser-treatment zone and considerably reduced banding pattern contrast (Fig. 8c, d), with the birefringence index as small as $(1.5 \pm 1) \times 10^{-3}$. A dark featureless area characteristic of an isotropic medium was observable at the sample surface. Note the spatial anisotropy of the laser-treatment area: the effect was more profound in the plane perpendicular to the long ligament axis (cf. Fig. 8a versus b; c versus d) in agreement with the elliptical damage profile determined by LM and SHG (Fig. 6).

DSC measurements revealed several notable differences between the laser-treated sample and the intact PL. In addition to the primary endothermic peak pertinent to intact PL, a lower-temperature peak at $T_{peak}^{L1} = 61.0 \pm 1.0°C$, $T_{onset}^{L1} = 58.5 \pm 1.5°C$ was detected for the L_1 group samples (Fig. 4b), curve L_1), whereas the total calorimetric enthalpy remained substantially unmodified $\left(\Delta H_m^{L1} = 63 \pm 2\,J/g\right)$ implying $\alpha = 0\%$. The experimental peaks were fitted to Lorentzians yielding total enthalpy percentage proportions of $18 \pm 5\%$ and $82 \pm 5\%$ corresponding to T_{peak}^{L1} and T_{peak}, respectively, where T_{peak} corresponded to that of intact PL. T_{peak}^{L2} manifested itself as a pronounced shoulder in Fig. 4b, curve L_2 causing a T_{onset}^{L2} downshift to $59.0 \pm 1.5°C$. The curve L_2 (Fig. 4b), curve L_2) changed markedly from the DSC curve of the intact PL (Fig. 4a) by the area plot A decrease (ΔH dropped to 35 ± 3 J/g) yielding a tangible
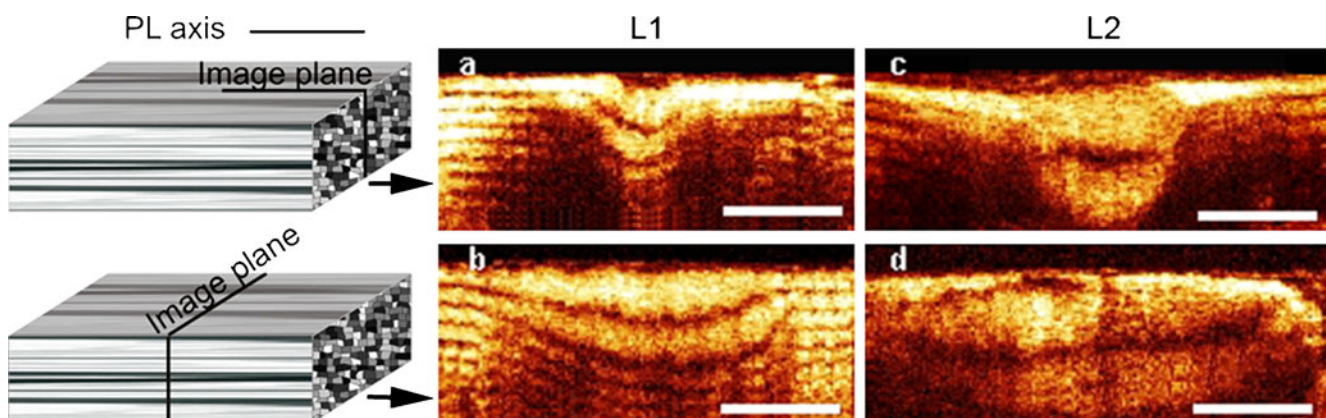

Fig. 8 CP-OCT images of laser-treated PL group samples: **a, b** L_1 and **c, d** L_2. Image planes were parallel and perpendicular to the PL axis in **a, c**, and **b, d**, respectively, as schematically presented in the *leftmost panel*. Scale bar, 500 μm

value of $\alpha = 55 \pm 5\%$, which was a measure of the collagen denaturation. An SI increase to 0.39 ± 0.03 ($p < 0.001$) was also noticeable.

Discussion

In situ structural modification of the collagenous tissue exposed to a dose of 100 J/cm^2 non-ablative laser radiation was studied. The overall process was complex due to the molecular and supramolecular interdependence of the collagen structure during and after the laser exposure. The choice of the high-purity collagen tissue helped to reduce this complexity. The main tissue content was type I collagen in triple helical conformation arranged in fibrous structures, as inferred from the biochemical, calorimetric, and optical assaying [11–13],[25–28]. Despite the high-collagen purity, the PL tissue still consisted of a variety of cellular and matrix components, such as cells, fibers, fascicles, bundles, and endotendineum sheaths. Moreover, two structural motifs coexisted in the ligament proper visualized as domains of smooth wavy and angular crimps reflecting the dual nature of the development and function of PL [17].

It was found that the laser-induced structural variations occurred at different levels of the PL tissue hierarchical organization ranging from the gross architecture to molecular state. In particular, the tissue anisotropic order was lost in a sub-millimeter vicinity of the treatment epicenter, as reported by CP-OCT. The high-hierarchy-level collagen network was profoundly disturbed in both L_1 and L_2 treatment groups. The collagen macromolecules retained the triple helical conformation (L_1) or underwent incomplete transition to a random coil state (L_2). At the same time, a less thermally stable population of collagen emerged, as inferred from a new low-temperature peak, T_{onset} decrease in L_1, and SI increase in L_2.

Importantly, it was found that both cells and collagen network damage extended well outside the epicenter (>2 mm) forming a penumbra (modified tissue outside of the laser spot), where temperature did not exceed 30°C. Four distinct morphological zones of the treated tissue were identified (Fig. 6). In the literature, two laser-treated tissue zones have been described as an epicenter and aura [29–32]. The innermost zone at the epicenter contained severely damaged collagen characterized by loss of the fibrillar structure, periodicity, and birefringence; the outermost zone contained tissue of partially compromised integrity: homogenized material, with inclusions of assorted collagen fibrils of normal and enlarged diameters. A complementary set of characterization techniques used in this work (LM/histology, SHG, CP-OCT imaging, and DSC) enabled refinement of the existing zonal model of the non-ablative laser treatment of collagenous tissue, including cross-comparison of the zonal and temperature maps. The cross-comparison of the thermometry and morphometry data provided strong evidence of the collagen structure modification in the vicinity of the laser spot, its periphery, and penumbra. Note that the L_1/L_2 zonal boundary did not conform to the laser spot (back-projected to the fiber aperture), or corresponding isotherms, as clearly seen in Fig. 6. In particular, the elliptical shape of the zones and their orientation perpendicular to the PL axis was counter-intuitive and should be emphasized. Obviously, these tissue macro-modifications were not due to the thermal effects alone.

Jacques [33] has proposed that thermo-mechanical stress plays an important role in the collagen network disturbance under non-uniform laser heating. Non-uniform thermo-elastic expansion of tissue and water accompanied by quasi-steady state stress build-up, expels interstitial fluid from the epicenter to the periphery of the porous solid matrix under the temperature and pressure gradient [15]. The transverse permeability of the ligament (i.e., across the PL axis) is small ($\sim 10^{-16}$ m$^4 \cdot$N$^{-1} \cdot$c^{-1}) [34] compared to a much higher (50-fold) longitudinal permeability [35] creating large local stress across the collagen fibrils and fibers that eventually results in their damage. At the same time, local thermal and mechanical stress along the PL axis is relaxed via fluid flow resulting in less tissue damage. The observed elliptical laser-treatment zones, with a long axis perpendicular to the PL axis, can be well interpreted in the framework of Jacques' model developed by others [31].

The hypothesis of the treated tissue shrinkage along the PL axis bulging out tissue in the perpendicular direction does not hold, since the collagen tissue shrinkage is known to be caused by the collagen denaturation, which was not the case in our experiments, as evident from Fig. 4.

Cellular necrosis and profound homogenization occurred in the two innermost zones, Z_1 and Z_2. Specifically, individual collagen structures, including fibers, fascicles, and bundles, were rendered poorly distinguishable. Such profound tissue homogenization at the given top temperatures is argued to be caused by a photothermal effect [33]. The reason for the heterogeneous material formation in Z_2 was two-fold: collagen swelling and fusion was governed by the photothermal effect, whereas the fibrous structure was split due to the thermo-mechanical effect. The damage extent was greater in L_2 due to the twice larger laser intensity at the same radiation dose (see Table 1), that emphasized the thermo-mechanical effect versus photothermal effect in L_2. However, collagen organization at the molecular and fibrillar levels reporting degradation degree could not be precisely determined by the H&E method due to the insufficient specificity of the matrix staining, and warrant further study by using SHG, DSC, and CP-OCT techniques.

Different degrees of damage of the collagen fibrous elements are illustrated in (Fig. 7e, f, g, h, and m, n, o, p)), as a dramatic loss of the SHG brightness and contrast due to the temperature rise at the epicenter (Z_1), and gradual regaining of intact PL appearance toward periphery (Z_2-Z_4). Since SHG was generated at the sub-wavelength structures scale (~200 nm) [18], the signal degradation in Z_1 reported disordering at the fibrillar level, rather than collagen molecule denaturation. Indeed, traces of the collagen fibrous structures were distinguishable at the very epicenter, in both L_1 and L_2, where $T_{max} < T_d$ and $T_{max} \geq T_d$, respectively. The DSC data further supported a hypothesis of the supra-molecular structural degradation rather than molecular denaturation, especially evident in L_1 (α=0%). In addition, a finite birefringence at the epicenter in L_1 reported incomplete degradation, as CP-OCT data demonstrated. In L_2, a temperature rise up to $67\pm2°C$ resulted in the unfolding of a fraction of the collagen molecules, as detected by DSC (ΔH decrease), also detectable as an isotropic (band-less) material in the CP-OCT images. This body of evidence suggested that the molecular collagen largely evaded denaturation. At the same time, cellular necrosis was unambiguously identified in Z_1 and Z_2 in both treatment groups, whereas only partial disintegration of the collagen fibrillar structure was found in the SHG images, thus ruling out coagulation as a possible mechanism explaining histologically observed homogenization. "Necrotic" and "coagulation" conditions were clearly defined in this work in terms of the cellular and matrix damage. Distinction of "necrosis" and "coagulation" has been also pointed out elsewhere [7]. Bedi et al. have shown that the collagen denaturation (coagulation) and necrotic zones were not equivalent [6].

In the DSC data, the appearance of a new T_{peak}^{L1} at the unchanged value of ΔH for the L_1 samples probably pointed to the formation of a destabilized collagen sub-population that contained triple-helical collagen macro-molecules. The SI increase in combination with the T_{onset}^{L1} decrease indicated that this sub-population persisted in both L_1 and L_2. This additional lower-temperature peak was reported to result from physical treatment of the collagenous samples [12],[36, 37]. The formation of a damaged intermediate state prior to the degradation of molecules to random coils has been proposed leading to reduction of the molecular stability due to the lattice structural damage. T_{peak}^{L1} (or SI increase) was interpreted as the collagen network disturbance (CP-OCT), accompanied by splitting of the collagen structures (LM, SHG). It is concluded that the enthalpy variation of the treated collagen sample was due to the supramolecular disorder. The thermo-labile collagen subpopulation was, probably, distributed across the laser-treated region. The calorimetric analysis provided strong support to the collagen network degradation (not the

molecule unfolding), as the main mechanism behind the non-ablative laser treatment.

The emergence of the pronounced angular crimps in Z_3 was surprising, especially in the L_1 group. The crimping period increased implying stretching of the tissue along the PL axis [17, 38, 39]. It is speculated that Z_3 acted as a cushion by absorbing mechanical stress between Z_4 and (Z_1 - Z_2).

It is worth pointing out the shortcomings of the reported methodology. The measured temperature and treatment patterns mismatched due to the difference in the respective temperature and treatment pattern acquisition depths. A quantitative model of the laser-treated collagenous tissue that captures its kinetic properties is needed, since the existing models are limited to the collagen denaturation at the molecular level, i.e., from the triple helices to random coils, disregarding supramolecular structural states. A more comprehensive model should include additional factors: anchoring of collagen fibers to the bones; intrinsic tension and applied load that stabilizes or destabilizes the collagen network [15, 40]. It is necessary to point out that this investigation addressed an ex vivo tissue whose physiological, optical, and morphological properties may differ from those of live tissues. Verification of the reported results in in vivo non-ablative treatment of PL tissue is important.

The DSC measurements were essentially non-local, hence unable to capture zonal specificity. Conventional histological analysis was cumbersome, invasive, essentially qualitative, and in general unable to report at the molecular level. Unlike transmission polarizing microscopy, CP-OCT was useful for determination of integral birefringence in reflection, although quantitative analysis of the connective tissue rearrangements remained challenging. SHG microscopy reported on supramolecular (especially fibrillar) organization levels, but was expensive, instrumentally complex, and difficult to interpret. At the same time, this technique has potential for morphological assessment of collagen tissue modification [41–43],[44].

Conclusions

In summary, a new phenomenological model of the collagenous tissue (e.g., *patella ligament*) degradation under non-ablative laser treatment was reported. The collagen structural integrity was compromised regressively by disintegration of bundles, followed by fibers, supramolecular fibrils, and, finally, collagen molecules. The reported zonal lesion pattern followed the progressive collagen network degradation pattern. Another surprising property of the laser-treated collagen tissue was the elliptical shape of the lesion, with the long axis across the patella ligament fiber axis. An existing model of the

molecular collagen denaturation alone was unable to explain this degradation diversity captured by imaging, histology, calorimetric, and bioassaying techniques. This model was revised to include the thermo-mechanical effect, which seemed to play the key role in the progressive degradation of the cells and collagen network, thus explaining the lesion zones. This study is believed to provide an insight into the non-ablative therapeutic laser treatment of the uniaxial connective tissue.

References

1. Niemz MH (2004) Laser-tissue interactions fundamentals and applications, 3rd edn. Springer, Berlin Heidelberg New York
2. Hayashi K, Peters DM, Thabit G, Hecht P, Vanderby R, Fanton GS, Markel MD (2000) The mechanism of joint capsule thermal modification in an in vitro sheep model. Clin Orthop Relat Res 370:236–249
3. Schaefer SL, Ciarelli MJ, Arnoczky SP, Ross HE (1997) Tissue shrinkage with the holmium:yttrium aluminum garnet laser—a postoperative assessment of tissue length, stiffness, and structure. Am J Sports Med 25(6):841–848
4. Hayashi K, Thabit G, Bogdanske JJ, Mascio LN, Markel MD (1996) The effect of nonablative laser energy on the ultrastructure of joint capsular collagen. Arthroscopy 12(4):474–481
5. Manstein D, Herron GS, Sink RK, Tanner H, Anderson RR (2004) Fractional photothermolysis: a new concept for cutaneous remodeling using microscopic patterns of thermal injury. Lasers Surg Med 34(5):426–438. doi:10.1002/lsm.20048
6. Bedi VP, Chan KF, Sink RK, Hantash BM, Herron GS, Rahman Z, Struck SK, Zachary CB (2007) The effects of pulse energy variations on the dimensions of microscopic thermal treatment zones in nonablative fractional resurfacing. Lasers Surg Med 39(2):145–155. doi:10.1002/lsm.20406
7. Agah R, Pearce JA, Welch AJ, Motamedi M (1994) Rate-process model for arterial tissue thermal-damage—implications on vessel photocoagulation. Lasers Surg Med 15(2):176–184
8. Aksan A, McGrath JJ, Nielubowicz DS (2005) Thermal damage prediction for collagenous tissues part i: a clinically relevant numerical simulation incorporating heating rate dependent denaturation. J Biomech Eng Trans Asme 127(1):85–97. doi:10.1115/1.1835355
9. Mandelkern L (2002) Crystallization of polymers vol 1, 2nd edn. Cambridge University Press, New York
10. McClain PE, Wiley ER (1972) Differential scanning calorimeter studies of the thermal transitions of collagen implication on structure and stability. J Biol Chem 247(3):692–697
11. Miles CA (1994) Differential scanning calorimetry (DSC)—protein-structure probe useful for the study of damaged tendons. Equine Vet J 26(4):255–256
12. Willett TL, Labow RS, Lee JM (2008) Mechanical overload decreases the thermal stability of collagen in an in vitro tensile overload tendon model. J Orthop Res 26(12):1605–1610. doi:10.1002/jor.20672
13. Vyazovkin S, Vincent L, Sbirrazzuoli N (2007) Thermal denaturation of collagen analyzed by isoconversional method. Macromol Biosci 7(11):1181–1186. doi:10.1002/mabi.200700162
14. Bischof JC, He X (2006) Thermal stability of proteins. Annals of the New York Academy of Sciences 1066:12–33. doi:10.1196/annals.1363.003
15. Ignatieva NY, Zakharkina OL, Andreeva IV, Sobol EN, Kamensky VA, Myakov AV, Averkiev SV, Lunin VV (2007) IR laser and heat-induced changes in annulus fibrosus collagen structure. Photochem Photobiol 83(3):675–685. doi:10.1111/j.1751-1097. 2007.00072.x
16. Kastelic J, Galeski A, Baer E (1978) The multicomposite structure of tendon. Connect Tissue Res 6(1):11–23
17. Franchi M, Raspanti M, Dell'Orbo C, Quaranta M, De Pasquale V, Ottani V, Ruggeri A (2008) Different crimp patterns in collagen fibrils relate to the subfibrillar arrangement. Connect Tissue Res 49(2):85–91. doi:10.1080/03008200801913635
18. Williams RM, Zipfel WR, Webb WW (2005) Interpreting second-harmonic generation images of collagen I fibrils. Biophys J 88(2):1377–1386. doi:10.1529/biophysj.104.047308
19. Xie TQ, Guo SG, Zhang J, Chen ZP, Peavy GM (2006) Determination of characteristics of degenerative joint disease using optical coherence tomography and polarization sensitive optical coherence tomography. Lasers Surg Med 38(9):852–865. doi:10.1002/lsm.20394
20. Srinivas SM, de Boer JF, Park H, Keikhanzadeh K, Huang HEL, Zhang J, Jung WQ, Chen ZP, Nelson JS (2004) Determination of burn depth by polarization-sensitive optical coherence tomography. J Biomed Opt 9(1):207–212
21. Kuranov RV, Sapozhnikova VV, Turchin IV, Zagainova EV, Gelikonov VM, Kamensky VA, Snopova LB, Prodanetz NN (2002) Complementary use of cross-polarization and standard OCT for differential diagnosis of pathological tissues. Opt Express 10(15):707–713
22. Cetta G, Tenni R, Castellani AA (1979) A simple method for quantitative estimation of collagen type III to type I ratio in soft tissues. Ital J Biochem 28(3):163–172
23. Blumenkrantz N, Asboe-Hansen G (1978) Hydroxyproline to hydroxylysine molar ratio indicates collagen type. Acta Dermatol Venereol 58(2):111–115
24. Tuchin VV (2007) Tissue optics: Light scattering methods and instruments for medical diagnosis, 2nd edn. SPIE Press, Bellingham, WA
25. Amiel D, Frank C, Harwood F, Fronek J, Akeson W (1984) Tendons and ligaments: a morphological and biochemical comparison. J Orthop Res 1(3):257–265
26. Graf BK, Fujisaki K, Vanderby R, Vailas AC (1992) The effect of insitu freezing on rabbit patellar tendon—a histologic, biochemical, and biomechanical analysis. Am J Sports Med 20(4):401–405
27. Rumian AP, Wallace AL, Birch HL (2007) Tendons and ligaments are anatomically distinct but overlap in molecular and morphological features—a comparative study in an ovine model. J Orthop Res 25(4):458–464. doi:10.1002/jor.20218
28. Matcher SJ, Winlove CP, Gangnus SV (2004) The collagen structure of bovine intervertebral disc studied using polarization-sensitive optical coherence tomography. Phys Med Biol 49(7):1295–1306. doi:10.1088/0031-9155/49/7/016
29. Kirsch KM, Zelickson BD, Zachary CB, Tope WD (1998) In: Ultrastructure of collagen thermally denatured by microsecond domain pulsed carbon dioxide laser. pp 1255-1259

30. Tang J, Godlewski G, Rouy S, Delacretaz G (1997) Morphologic changes in collagen fibers after 830 nm diode laser welding. Lasers Surg Med 21(5):438–443

31. Zweig AD, Meierhofer B, Müller OM, Mischler C, Romano V, Frenz M, Weber HP (1990) Lateral thermal damage along pulsed laser incisions. Lasers Surg Med 10:262–274

32. Matteini P, Ratto F, Rossi F, Cicchi R, Stringari C, Kapsokalyvas D, Pavone FS, Pini R (2009) Photothermally-induced disordered patterns of corneal collagen revealed by SHG imaging. Opt Express 17(6):4868–4878

33. Jacques SL (1992) Laser tissue interactions—photochemical, photothermal, and photomechanical. Surg Clin North Am 72 (3):531–558

34. Weiss JA, Maakestad BJ (2006) Permeability of human medial collateral ligament in compression transverse to the collagen fiber direction. J Biomech 39(2):276–283. doi:10.1016/j.jbiomech. 2004.11.016

35. Chen CT, Malcus DS, Vanderby R Jr (1998) A fiber matrix model for interstitial fluid flow and permeability in ligaments and tendons. Biorheology 35(2):103–118

36. Miles CA, Sionkowska A, Hulin SL, Sims TJ, Avery NC, Bailey AJ (2000) Identification of an intermediate state in the helix-coil degradation of collagen by ultraviolet light. J Biol Chem 275 (42):33014–33020

37. Bognar G, Szabo I, Balint L, Hepp B, Kereskai L, Lorinczy D (2007) Thermal effects of shoulder electrothermal arthroscopic capsulorrhaphy monitored by differential scanning calorimetry—a preliminary study. Thermochim Acta 464(1–2):78–82. doi:10.1016/j.tca.2007.07.020

38. James R, Kesturu G, Balian G, Chhabra AB (2008) Tendon: biology, biomechanics, repair, growth factors, and evolving treatment options. J Hand Surg Am 33A(1):102–112. doi:10.1016/j.jhsa.2007.09.007

39. Cribb AM, Scott JE (1995) Tendon response to tensile-stress—an ultrastructural investigation of collagen–proteoglycan interactions in stressed tendon. J Anat 187:423–428

40. Wells PB, Thomsen S, Jones MA, Baek S, Humphrey JD (2005) Histological evidence for the role of mechanical stress in modulating thermal denaturation of collagen. Biomech Model Mechanobiol 4(4):201–210. doi:10.1007/s10237-005-0002-1

41. Kim BM, Eichler J, Reiser KM, Rubenchik AM, Da Silva LB (2000) Collagen structure and nonlinear susceptibility: effects of heat, glycation, and enzymatic cleavage on second harmonic signal intensity. Lasers Surg Med 27(4):329–335

42. Sun Y, Chen WL, Lin SJ, Jee SH, Chen YF, Lin LC, So PTC, Dong CY (2006) Investigating mechanisms of collagen thermal denaturation by high-resolution second-harmonic generation imaging. Biophys J 91(7):2620–2625. doi:10.1529/biophysj. 106.085902

43. LaComb R, Nadiarnykh O, Campagnola PJ (2008) Quantitative second harmonic generation imaging of the diseased state osteogenesis imperfecta: experiment and simulation. Biophys J 94(11):4504–4514. doi:10.1529/biophysj.107. 114405

44. Tan HY, Teng SW, Lo W, Lin WC, Lin SJ, Jee SH, Dong CY (2005) In: Characterizing the thermally induced structural changes to intact porcine eye, part 1: Second harmonic generation imaging of cornea stroma. doi:10.1117/1.2012987